MAGNETIC RESONANCE IN MEDICINE 2, 555–566 (1985)

Magnetic Resonance Imaging the Velocity Vector Components of Fluid Flow*

DAVID A. FEINBERG, LAWRENCE E. CROOKS, PHILLIP SHELDON, JOHN HOENNINGER III, JEFFREY WATTS, AND MITSUAKI ARAKAWA

Radiologic Imaging Laboratory, University of California, 400 Grandview Drive, San Francisco, California 94080

Received January 2, 1985; revised April 10, 1985

Encoding the precession phase angle of proton nuclei for Fourier analysis has produced accurate measurement of fluid velocity vector components by MRI. A pair of identical gradient pulses separated in time by exactly ½ TE, are used to linearly encode the phase of flow velocity vector components without changing the phase of stationary nuclei. Two-dimensional Fourier transformation of signals gave velocity density images of laminar flow in angled tubes which were in agreement with the laws of vector addition. These velocity profile images provide a quantitative method for the investigation of fluid dynamics and hemodynamics. © 1985 Academic Press, Inc.

Since the earliest observations by Suryan (*1*) of NMR signals arising from water flowing in tubes, there has been considerable interest in applying magnetic resonance (MR) to image blood flow. One immediate application of MR velocity imaging is the study of hemodynamics of the human cardiovascular system. In medical applications, if magnetic resonance imaging is capable of showing the velocity and patterns of blood flow, it could be used to assess tissue and organ perfusion, patency of vascular grafts, and for detection of intraarterial plaque. Investigators have applied NMR spectroscopy to measure mean velocity rates of fluid (*2*) and of blood flow *in vivo* (*3*). MRI techniques have been used to study flow-related changes in the magnitude of signal which are dependent on the filling time of blood into imaged planar volumes (*4–6*). Time of flight techniques in conjunction with even echo phase coherence (*7*) have shown mean blood velocity in human arteries separate from static tissue. All of the above techniques measure mean flow velocity by the quantitation of signal magnitude.

NMR flow velocity measurements based on quantitation of signal phase have developed concurrently with signal magnitude techniques (*8–13*). In theoretical work, Hahn (*8*) showed the dependence of the NMR precession phase angle on flow in the direction of a magnetic field gradient. Other investigators have demonstrated the velocity distribution of fluid flow (*10*) and of blood flow, *in vivo* (*11*) by Fourier transformation of phase-encoded NMR signals. Recently, it has been demonstrated that bipolar gradient pulses can be incorporated into imaging sequences to phase encode

* Presented at the Third Annual Meeting of the Society of Magnetic Resonance in Medicine, New York, N.Y., August 13–17, 1984. Supported by Diasonics Inc.–MRI Division.

0740-3194/85 $3.00

a component of velocity (*12*). Also reported recently is an imaging sequence which phase encodes velocity in spin-echo images without altering the phase of stationary nuclei (*6*), utilizing a pair of identical gradient pulses separated in time by a interval equal to the 90 and 180° rf pulse separation, TE/2. In the experiments reported here, several pairs of TE/2 periodic gradient pulses are incorporated in a spin-echo image sequence to define components of the velocity vector of flow (*13*).

THEORY

An isochromate is defined as a small fluid volume which is large enough for its net magnetic vector to obey the classical Bloch equations yet small enough to have negligible variations of the magnetic field across its volume. Because of its size relative to a tube or blood vessel, an isochromatic group within an image element (voxel) is composed of nuclear moments having different velocities. The net magnetic moment $\mathbf{M}(t)$ of an isochromatic group at the time of spin-echo rephasing is proportional to the integral of all nuclear moments in the group,

$$\mathbf{M}(t) = K \int_{-\infty}^{+\infty} D(\mathbf{V}) \cdot e^{\angle \varphi(\mathbf{V})} \cdot d\mathbf{V} \qquad [1]$$

where φ is the phase of an individual nuclear moment at a specific time, velocity and position, and K is a proportionality constant dependent on coil geometry, receiver gain, and other imaging system-specific parameters. The number of nuclei having velocity between $\mathbf{V}$ and $\mathbf{V} + d\mathbf{V}$ is defined as $D(\mathbf{V})$, the velocity density. The measurement of a velocity profile is based on the change in the precession phase angle $\varphi(\mathbf{V})$ of the spin-echo signal due to the movement of nuclei along the direction of an applied magnetic gradient,

$$\varphi(\mathbf{V}) = \int_{t_1}^{t_1+\delta} \gamma \mathbf{G}(t) \cdot (\mathbf{V}t + \mathbf{r}_0) dt \qquad [2]$$

where γ is the gyromagnetic ratio, $\mathbf{r}_0$ is the initial position of the spin nuclei, δ is the duration of the gradient pulse, and t_1 is the time between the 90° rf pulse and the first TE/2 periodic gradient pulse. To produce a velocity density image of a vector component of flow, a pair of gradient pulses with identical strength and pulse duration are applied before and after the first 180° nutation rf pulse, Fig. 1. As is shown below, the two gradient pulses must be separated in time by TE/2 or τ so that the net phase accumulated by nuclei moving at constant velocity and stationary nuclei is zero during the second echo. Integration of Eq. [2] gives the net phase shift accumulated during the first of the two gradient pulses,

$$\varphi(t_1 + \delta) = \gamma \mathbf{G} \cdot (\mathbf{V}\delta^2/2 + \mathbf{V}\delta t_1 + \delta \mathbf{r}_0). \qquad [3]$$

Prior to the second gradient pulse, the 180° rf pulse nutates the spins and changes the sense of phase,

$$\varphi(\tau) = -\varphi(t_1 + \delta). \qquad [4]$$

After the second gradient pulse, the net accumulated phase of any static nuclei is zero (see Fig. 1B). Therefore, at the time of spin echo, TE, the phase shift accumulated by the spins is directly proportional to the velocity and to the applied gradient,

$$\varphi(\mathrm{TE}) = \gamma G \delta \mathrm{TE}/2\mathbf{V}. \qquad [5]$$

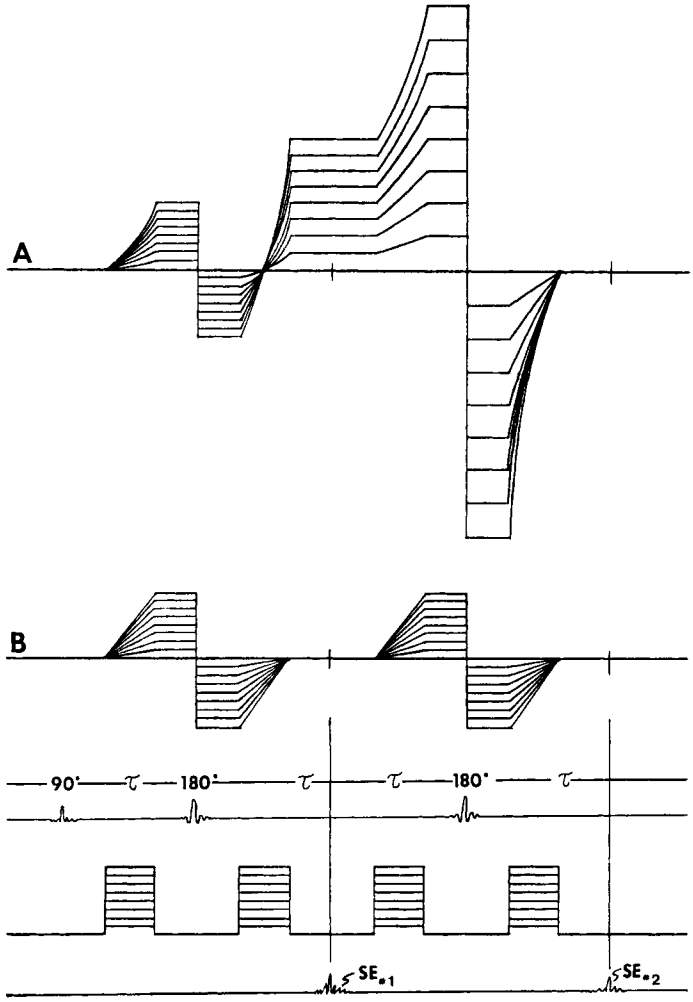

FIG. 1. Principle of encoding the phase of the transverse magnetization vector with a pair of linear gradient pulses spaced in time by TE/2. Plots of phase versus time are shown (A) for nuclei moving with a velocity component along the gradient axis and (B) for static nuclei at a nonzero position. The net phase of the moving nuclei at TE is shown to change linearly with the strength of the gradient pulses, while the net accumulated phase of static nuclei at the time of echo is always zero.

This phase shift, Eq. [5], can be substituted into Eq. [1] for a general expression of the phase-encoded spin-echo signal,

$$\mathbf{M}(\mathrm{TE}) = K \int_{-\infty}^{+\infty} D(\mathbf{V}) \cdot e^{i(\delta \cdot G \cdot \delta \cdot \mathrm{TE}/2 \cdot \mathbf{V})} d\mathbf{V}. \qquad [6]$$

To encode the spatial position of the nuclei, linear magnetic gradient, G_x is applied during the signal readout period. In the presence of G_x both resonance frequencies of flowing nuclei and static nuclei become linearly dependent on their position, r_x, along the x axis. Phase is encoded with dependence on the velocity vector component V_y

by the TE/2 periodic gradient pulses of G_y. The net magnetization vector can be expressed in terms of velocity and spatial location,

$$\mathbf{M}(t, \gamma \cdot G_y \cdot \mathrm{TE}/2) = K \int_{-\infty}^{+\infty} \int_{-\infty}^{+\infty} D(V_y, r_x) e^{-i\gamma(G_y \delta \mathrm{TE} V_y/2 + G_x t r_x)} \cdot dV_y dr_x. \quad [7]$$

Since the phase shift is directly proportional to the velocity vector component V_y, either the TE/2 periodic gradient strength or pulse duration can be incrementally changed to phase encode the signal. In these experiments, 128 different strengths of the gradient pulses were used to linearly encode the phase of spin-echo signals. A 2D-Fourier transformation of these signals gives the image intensity, $D(V_y, r_x)$, which is the relative number of nuclei flowing at a particular velocity and spatial location in the image.

$$D(V_y, r_x) = \frac{K'}{2\pi} \int_{-\infty}^{\infty} \int_{-\infty}^{\infty} M\left(t, \frac{1}{2}\gamma G_y \cdot \mathrm{TE}\right) \times e^{-i\gamma(G_y \cdot \delta \cdot \mathrm{TE}/2 \cdot V_y + G_x \cdot t \cdot r_x)} \cdot d\left(\frac{1}{2}\gamma G_y \delta \cdot \mathrm{TE}\right) d(\gamma G_x t). \quad [8]$$

As shown in Fig. 2, the image section's thickness is determined by sinc-modulated rf pulses in the presence of slice selective Z-gradient pulses. The spatial resolution is produced by the G_x gradient present during the spin-echo readout period. It should be noted here that an additional linear phase encoding of static nuclei and application of a 3D FT would resolve the velocity density over two spatial axes instead of a projected planar volume. Image acquisition time for these 2D FT experiments was 2 or 4 min in cardiac-gated mode. A similar field of view and resolution in a 3D FT experiments, however, would have taken 128 times longer or 2–4 h.

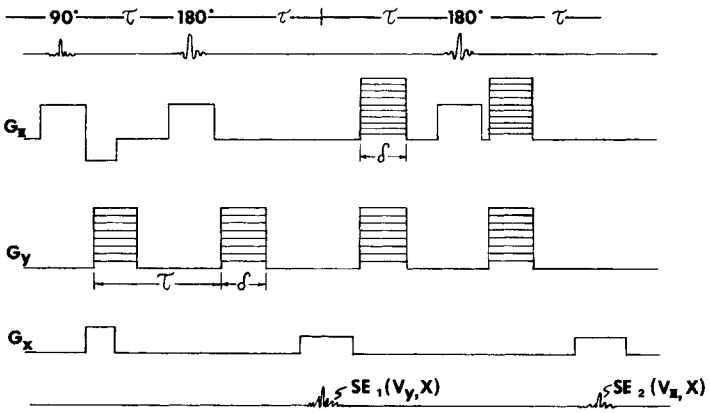

FIG. 2. The pulse sequence used to encode a spin-echo velocity measurement for Fourier phase analysis. The diagram shows timing of the three orthogonal gradient directions (G_x, G_y, G_z), the sinc-modulated radiofrequency pulses (rf), and the spin-echo signals (SE). Changes in the gradient strength are illustrated by horizontal striped lines in the TE/2-periodic phase-encoding gradient pulses; these six gradient pulses are incrementally increased through 128 different gradient strengths in the 128 interactions of this pulse sequence. Spatial information is determined by the x gradients on during the two spin-echo sampling times at 2τ and 4τ. The G_z gradient pulses present during the three rf pulses determine the image volume thickness.

A velocity profile of V_z was encoded on the second spin echo with the following method. A second pair of TE/2 periodic G_y pulses was placed about the second 180° nutation rf pulse so that the net phase accumulation during the 4 G_y pulses is zero. The V_z is encoded on the second spin echo with a pair of TE/2 periodic G_z pulses applied simultaneous with the second pair of G_y pulses, as is shown in Fig. 2.

METHODS

The pulse sequences were developed and implemented on a whole body imaging system operating at 3.5 kG field strength. The system is equipped with three sets of orthogonal gradient coils; a Cartesian coordinate system is defined with the z axis along the direction of the static magnetic field (the long axis of the patient), y axis is the vertical direction, and the x axis in the horizontal direction. The velocity vector components V_x, V_y, and V_z are defined with respect to this orthogonal coordinate system.

The flow phantom shown in Fig. 3A, consisted of eight plastic tubes connected in series and immersed in a water-filled box. Four pairs of identical diameter tubes were arranged horizontally in order of decreasing diameters from right to left: 1.27, 0.9525, 0.68, 0.31 cm ($\frac{1}{2}$, $\frac{3}{8}$, $\frac{1}{4}$, $\frac{1}{8}$ in.). The tubes were arranged with one set of different diameter tubes in the horizontal plane of the z axis, and the second set oriented at 23.9° with respect to the z axis in the z–y plane. All eight tubes were connected in series by several meters of flexible tubing, long enough for magnetic polarization of the fluid during the time between successive passes through the phantom. A variable speed pump, placed outside of the rf-shielded screen room, pumped fluid in the same direction through all of the phantom's tubes, with downward-directed flow in the angled set of tubes. The fluid was a solution of demineralized water with methyl cellulose added for increased viscosity, and copper sulfate added for T_1 relaxation similar to whole blood. The fluid viscosity of 6.5 cp was set within the normal range of whole blood viscosity, 5–7 cp. The volume flow rate (Q) was 448 ml per minute, as measured by timed collections of fluid volume and by flow meters (*14*) attached in the return path of the pump. Due to the tubes being connected in series the velocity was inversely proportional to each tube's cross-sectional area. The velocities were intended to be within the range of intravascular blood velocities, (5 to 100 cm/s).

Laminar flow in a radially symmetric tube has a well-known parabolic velocity profile of $V = 2 \cdot V_{avg}(1 - b^2/r^2)$ where V_{avg} is the average velocity, r is the radius, and b is the radial distance from the center of a circular cross-section (*15*). The maximum velocity V_{max}, in the center of the tube is two times the average velocity, or $V_{max} = 2 \cdot Q/A$ where Q is the volume flow rate and A is the cross-sectional area of each tube. Assuming laminar flow, the velocity density images were calibrated by setting the calculated V_{max} of the horizontal 0.952-cm-diam tube (21 cm/s) to the peak height of its image profile, giving the calibration scale (cm/s/pixel).

The images' velocity range could be increased by displacement of the signal refocusing volume in the direction of flow (*7*). A planar volume was selectively irradiated by a sinc-modulated 90° nutation rf pulse in the presence of a pulsed linear magnetic gradient on the z axis. A spatially selective sinc-modulated 180° rf pulse with its frequency shifted from the 90° pulse was applied in presence of a pulsed Z gradient. The frequency offset resulted in spatial displacement of the refocusing volumes by 3

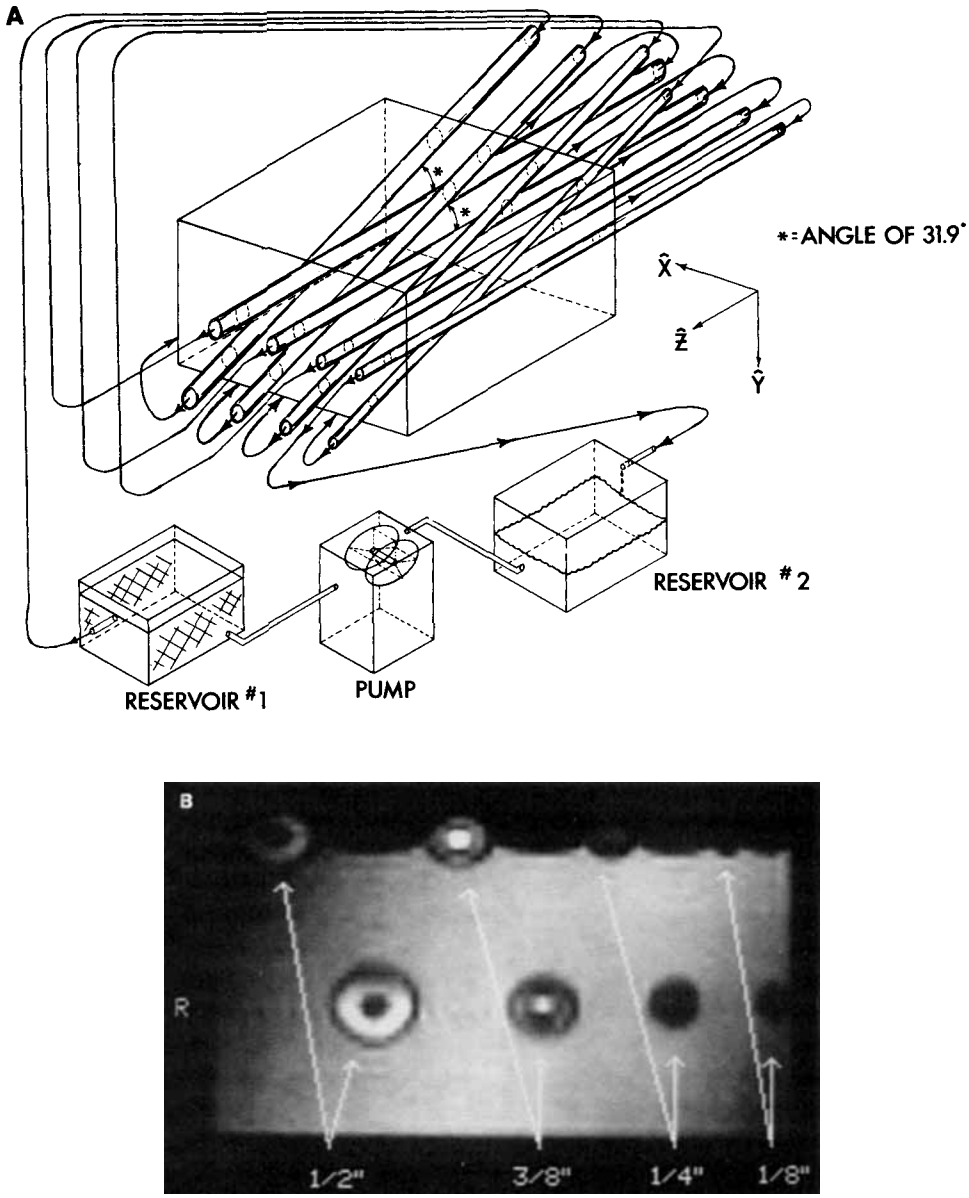

FIG. 3. (A) Diagram of flow phantom shows direction of flow and the orientation of the two sets of tubes at 23.9° with respect to each other. (B) Magnitude image of flow phantom shows the position of tubes. Signal from the flowing nuclei is apparent in several of the larger diameter tubes.

and 12 mm along the z axis for the first and second spin echos (SE), respectively. To visualize the signal magnitude of fluid flowing in the phantom, a velocity-dependent image, Fig. 3B, was generated with displacement in the direction of flow. Using this displacement technique, the velocity profiles were made in a 1.0-cm-thick planar vol-

ume with 0.75-mm spatial resolution on the x axis (Figs. 4A, B). The refocusing pulses were displaced by 3 and 9 mm in the $+z$ direction with TE equal to 66 ms. The imaging time was 2 min. Figure 4C shows the V_y velocity profile of the phantom when an air bubble was trapped at the entrance orifice of the second from left tube. A faint signal band directed vertically is visual.

To image pulsatile blood flow in human arteries, each cycle of the pulse sequence was synchronized to the cardiac cycle. Either a laser Doppler flow meter (*16*) or an electrocardiogram (EKG) monitor (*17*) was employed for synchronization to the cardiac cycle in different imaging experiments. With both methods, an optic fiber was used to transmit the gating signal out of the rf shield room to an electronic delay unit for triggering the beginning of each iteration of the imaging sequence.

A velocity profile, V_y, of the abdominal aorta was acquired near the time of peak flow at 300 ms delay after the R wave using the EKG monitor for synchronization (Figs. 5A, B). The velocity profile image was calibrated with the phantom experiments. The imaging time for cardiac-gating experiments was typically 4 min. The signal from stationary tissue is not phase encoded by the TE/2-periodic gradient pulses and therefore appears as a bright horizontal band in Fig. 5B at the vertical position of zero velocity.

DISCUSSION

The parabolic shape of each velocity profile Figs. 4A, B is consistent with a theoretically predicted laminar flow profile in which the velocity varies proportional to the square of the radial position. The MRI velocity profiles vary in height according to the velocity magnitude and to the laws of vector addition. In Fig. 4A, only the tubes angled on the y axis showed velocity density. The faintness of signal intensity in velocity profiles of the 0.68-cm-diam tubes (at the extreme right in the two images) probably resulted from the movement of magnetically tagged protons beyond the displaced volume of the refocusing plane. Similarly, no profiles are seen for the smallest diameter tubes (0.31 cm diam) in which the velocity is greatest. Nevertheless, velocity images could be adjusted to higher velocity ranges either by increasing the thickness of the planar volumes by increasing the displacement between the volumes of excitation and refocusing, or by applying 180° rf nutation pulses without slice-selective gradient pulses. The effect of turbulence on the tubes' velocity profile is shown in Fig. 4C, where the abrupt narrowing of the tube lumen produced eddies in the flow pattern at the downstream location of the image plane.

The quantitative results of the tube phantom studies are shown in Table 1. It should be noted that the tubes of different diameters were connected in series so all had the same volumetric flow with each tube's average and maximum velocity inversely proportional to their different cross-sectional areas. The volume flow rates measured from the imaged velocity vector components have a mean value of 442 ± 28.6 ml/min which is close to the independent volumetric measurement of 448 ml/min. Calculating the arc tangent of the velocity vector components in the angled tubes gave an average angle measurement of 23.0 ± 0.1° which compared favorably with 23.9° directly measured on the tube phantom.

By combining the above displacement technique with the Fourier phase-encoding technique, the V_y velocity profile of blood flow in the abdominal aorta was measured at 23 cm/s. The profile appeared to be nearly flat across the lumen of the vessel in

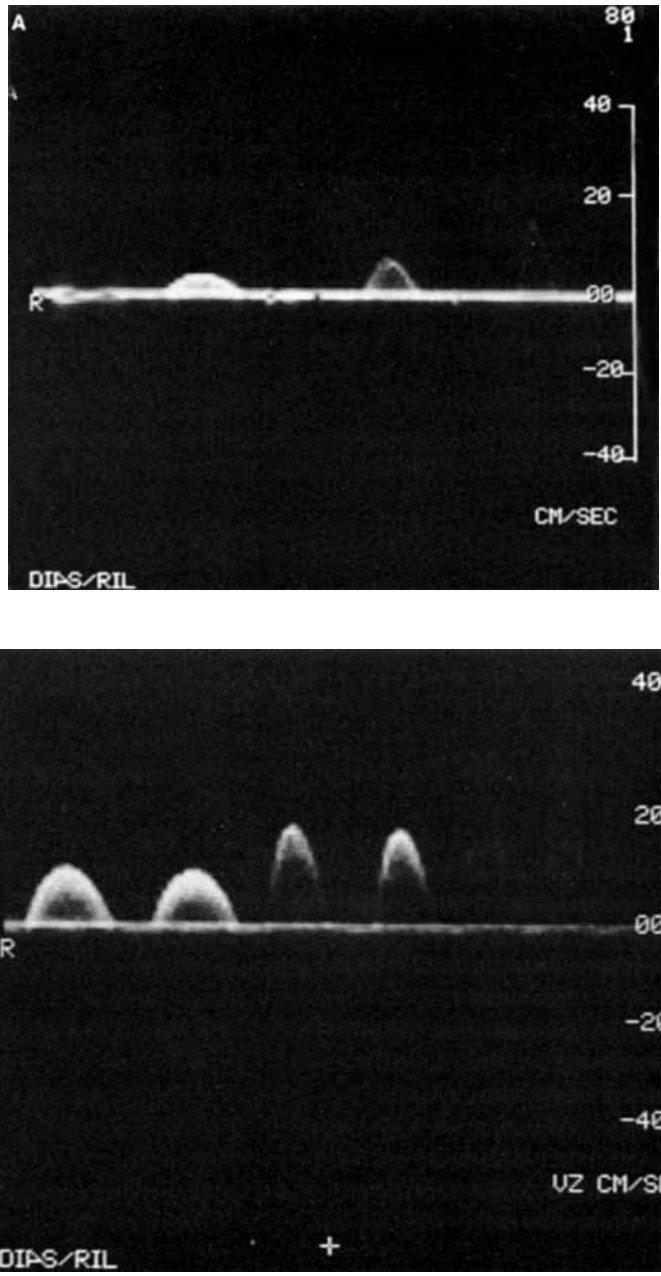

FIG. 4. Magnetic resonance images of velocity vector components, V_y and V_z, of fluid flowing in different diameter tubes. The velocity density is displayed in each image as a function of velocity in the vertical direction and position, r_x, in the horizontal direction. The two spin-echo images have spatial resolution on the x axis horizontal across the images, and velocity resolution in the vertical direction. The V_y velocity profiles (A) appear only in the tubes which are angled in the y–z plane. The V_z velocity profiles (B) are present for the angled tubes and the tubes which are parallel to the z axis. The velocity profile height is inversely proportional to the cross-sectional area of each tube, all of which have the same volume flow rate. The very faint signal in the velocity profiles on the right is caused by the tagged nuclei moving out of the refocusing volume. (C) Demonstration of a turbulent flow artifact which occurred when an air bubble was trapped at the top inflow orifice of the second tube from left.

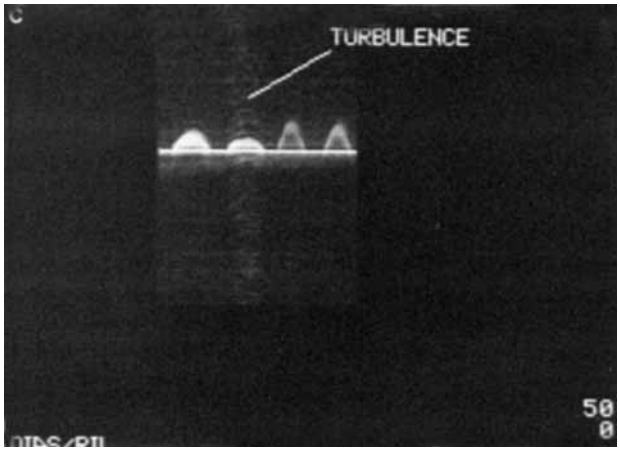

FIG. 4—*Continued.*

Fig. 5B. This flat velocity profile called "plug flow" is known to occur in elastic-walled large-diameter blood vessels during pulsatile flow (*18*). When the Womersley number becomes large, as is true for large-diameter blood vessels such as the aorta, the velocity profile is blunt, in contrast to the parabolic-shaped profiles of Poiseuillean flow. At this end systolic phase of the cardiac cycle, turbulent flow might also occur due, in part, to a decreased stability of flow during its deceleration (*19*). The effect of turbulence on this MR imaging technique is to disrupt the linearity of the phase-encoding process, producing a spreading of signal on the images velocity axis, as shown in Fig. 4C. Similarly, the presence of turbulence could explain the faint band of signal spread over the region of the aortic velocity profile. This faint band may also have been caused by cycle-to-cycle variations in velocity between the several cardiac cycles of the total imaging time, or perhaps by vessel wall motion.

The choice of technique for synchronization of the pulse sequence to pulsatile flow depends in part on the location of the blood vessels in the body, the cardiac cycle phase, as well as the suitability of the synchronization apparatus to the magnetic field and radiofrequency environment. The battery-powered EKG monitor gave nearly direct synchronization to the contraction of heart ventricles and is excellent for cardiac imaging; however, the EKG permitted only indirect synchronization to the very fast pulse wave in the aorta. Additional impedence changes at vessel bifurcations would further reduce the reliability of EKG signal's synchronicity to flow in the head and limbs.

One significant difference between the technique of phase-encoding velocity in MR images and techniques dependent on signal magnitude measurement is the problem associated with partial volume averaging of stationary tissue with flowing blood. With either a single phase image or with most magnitude imaging techniques, stationary tissue can become partial volume averaged with the intravascular blood in image elements, particularly if the blood vessel lies diagonal to the chosen axis of velocity resolution. Consequently, the accuracy of measuring velocity is severely reduced. With this Fourier phase-encoding technique, however, signal from even very large partial

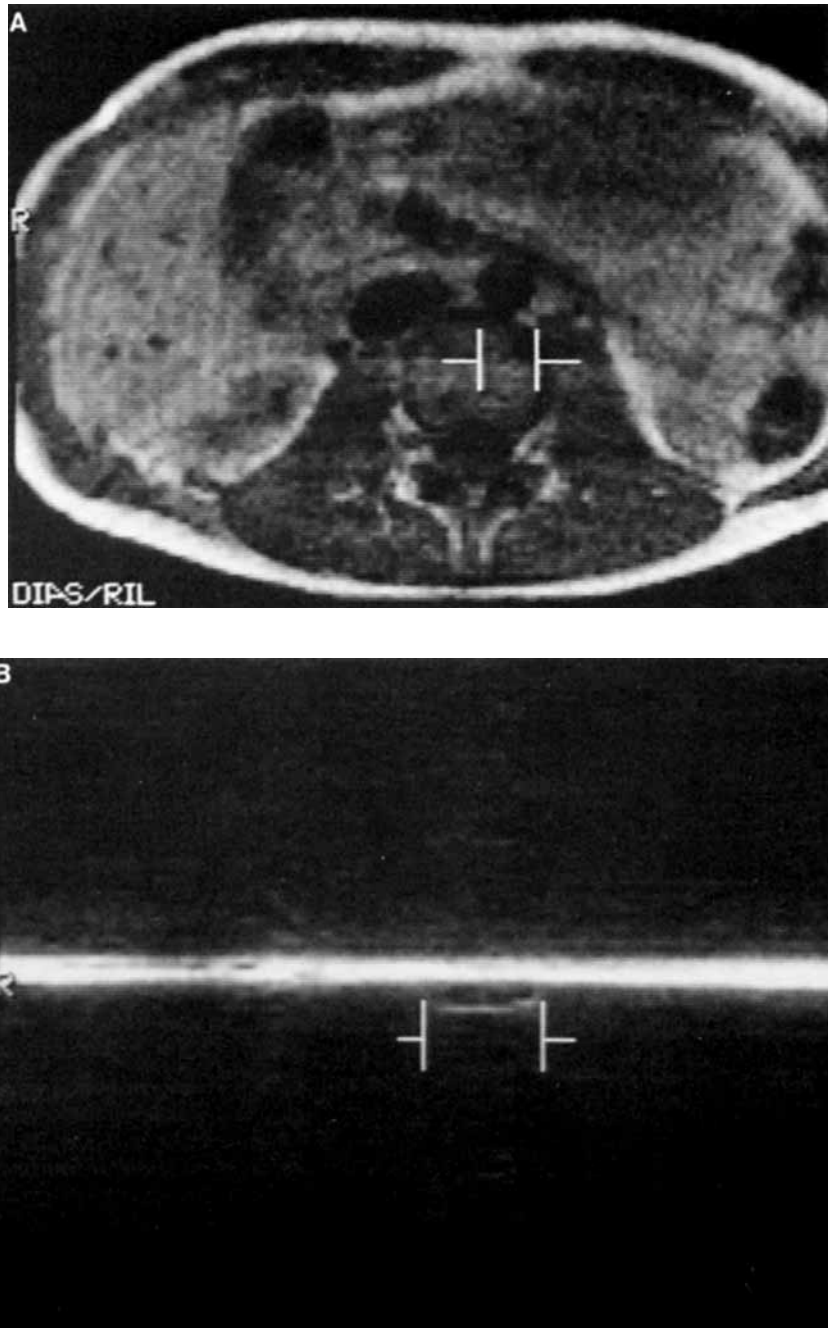

FIG. 5. Transverse two-dimensional image of the abdomen (A). Blood flowing in the aorta does not produce a high signal in the conventional spin-echo image without cardiac synchronization. Figure 4B is a one-dimensional image of the velocity vector component, V_y, recorded at 300 ms delay after the heart's R wave using an EKG monitor to synchronize the pulse sequence to the cardiac cycle. Here V_y is 23 cm/s across much of the vessel's lumen. Such a flat velocity profile for the aortic blood flow is as predicted for large elastic walled vessels during pulsatile flow. The brackets, positioned directly below the aorta in (A) demark the same location on the x axis in (B) where the velocity profile is located. (B) Twice the scale of (A).

TABLE 1

The Maximum Velocities, V_y and V_z, of the Six Imaged Tubes and Their Diameter and Cross-Sectional Area

	Diameter (cm)	Area (cm^2)	V_y (cm/s)	V_z (cm/s)	$\sqrt{V_y^2 + V_z^2}$ (cm/s)	$\tan^{-1}(V_y/V_z)$ (°)	Q (ml/min)
Tubes in y–z plane	0.68	0.363	17.7	40.9	44.5	23.4	485
	0.952	0.71	8.3	18.8	20.5	23.8	438
	1.27	1.267	4.42	11.0	11.8	21.9	448
Horizontal tubes	0.68	0.63	0.0	—	—	0.0	—
	0.952	0.712	0.0	21.0*	21.0	0.0	448[a]
	1.27	1.267	0.0	11.0	11.0	0.0	418
						Mean ± SD	
						23.0 ± 1.0 (n = 3)	442 ± 28.6 (n = 4)

Note. Shown are the calculated angles of each tube and their measured volume flow rate, Q, calculated from the cross-sectional area and the measured velocity magnitude, $\sqrt{V_y^2 + V_z^2}$, as defined in the text. An independent measurement of the volume flow rate made with a flow meter and timed volumetric measurements was 448 ml/min, and the actual angle of the tubes in the y–z plane was 23.9°. The maximum velocity in the horizontal 0.68-cm tube could not be measured in Fig. 3B.

[a] The horizontal 0.952-cm tube was used to calibrate the velocity measurements, and therefore was excluded from the mean measurement of flow rate, Q.

volumes of static tissue is not phase encoded and therefore stationary tissue does not affect the accuracy of the velocity measurement. Separation of the velocity density distribution from stationary tissue's signal (the horizontal band of signal at zero velocity in Figs. 4 and 5) is well demonstrated in these experiments. Imaging the capillary blood flow of organs, tissue perfusion, separate from large partial volumes of static tissue therefore might be possible with this Fourier phase-encoding technique.

CONCLUSION

In accordance with the Pythagorean theorem and within experimental error, the magnitude of the sum of the two velocity vector components in angled tubes is equal to the magnitude of the velocity in identical diameter tubes placed along the horizontal axis. This result is unaffected by possible errors in calibration of velocity by a scalar constant and demonstrates the internal consistency and accuracy of the MRI velocity vector measurements. In conclusion, the MRI velocity density images of fluid flow are in agreement with the Newtonian laws of motion and the laws of vector addition. Our studies show that this MR Fourier imaging technique provides quantitation of fluid velocity and shows flow patterns without perturbing the system dynamics.

ACKNOWLEDGMENT

The authors gratefully acknowledge the design and execution of the illustrations by Gary Temkow.

REFERENCES

1. G. SURYAN, *Proc. Indian Acad. Sci., Sect. A* **33,** 107 (1951).
2. J. H. BATTOCLETTI, R. HALBACH, S. SALLES-CUNHA, AND A. SANCHES, JR., *Med. Phys.* **8,** 435 (1981).
3. J. R. SINGER, *Science (Washington, D.C.)* **130,** 1652 (1959).

4. L. KAUFMAN, L. E. CROOKS, P. E. SHELDON, W. ROWAN, AND T. MILLER, *Invest. Radiol.* **17**(6), Dec. (1982).
5. J. R. SINGER AND L. E. CROOKS, *Science (Washington, D.C.)* **221,** 654 (1983).
6. D. A. FEINBERG, *Magn. Reson. Med.* **1,** 151 (1983) (Abstract).
7. D. A. FEINBERG, L. E. CROOKS, J. HOENNINGER, M. ARAKAWA, AND J. WATTS, *Radiology* **153**(1), 177 (1984).
8. E. L. HAHN, *J. Geophy. Res.* **65,** 776 (1960).
9. K. J. PACKER, *Mol. Phys.* **17,** 353 (1969).
10. A. N. GARROWAY, *J. Phys. D* **7,** 159 (1974).
11. T. GROVER AND J. R. SINGER, *J. Appl. Phys.* **42,** 938 (1971).
12. T. W. REDPATH, D. G. NORRIS, R. A. JONES, AND J. M. S. HUTCHISON, *Phys. Med. Biol.* **29,** 891 (1984).
13. D. A. FEINBERG, L. CROOKS, J. HOENNINGER, M. ARAKAWA, J. WATTS, in "Proceedings, Third Annual Meeting of the Society of Magnetic Resonance in Medicine, New York, New York, August 17–23, 1984."
14. "Variable Area Flow Meters, FM044-40ST," Cole–Parmer Instrument Co., Chicago, Ill.
15. W. HERMS, *Ann. Phys. (Leipzig)* **8,** 280 (1961).
16. Med. Pacific LD 5000 Laser Doppler Flow Meter.
17. Diasonics Cardiac Gating Monitor.
18. D. A. MCDONALD, "Blood Flow in Arteries," Arnold, London, 1974.
19. W. A. SEED AND N. B. WOOD, *Cardiovasc. Res.* **5,** 319 (1971).